Separability of Systematic Effects in Polarimetric GNSS Radio Occultations for Precipitation Sensing

Sergio Tomás, Ramon Padullés, and Estel Cardellach, *Member, IEEE*

Abstract— The Global Navigation Satellite System (GNSS) polarimetric effects on the propagation of radio occultations (ROs) are studied here. Polarimetric ROs have been suggested as a technique to detect heavy rain events using opportunity signals from GNSS satellites. The systematic effects that hinder the isolation of the precipitation information are described and their significance and separability are assessed. A method that relies on the received phase difference between polarizations is presented. A dual-frequency extension is capable to completely separate the hydrometeor information from the other effects, including the ionospheric influence.

Index Terms— Faraday effect, Global Navigation Satellite System (GNSS), microwave propagation, polarimetry, radio occultation (RO), rainfall effects.

I. INTRODUCTION

THE radio occultations (ROs) of Global Navigation Satellite System (GNSS) opportunity signals constitute a measurement technique for atmospheric sounding (see [1], [2]). They provide vertical refractivity profiles from the delay and bending of radio links when the transmitter rises or sets above/below the earth horizon. These profiles in turn allow the retrieval of thermodynamic properties as pressure, temperature, and water vapor. Compared with other instrumentation such as radiosondes or weather satellites, the GNSS-RO observations present lower systematic errors [3]. Thus, they have become a reliable data source to be assimilated operationally into numerical weather prediction models with no bias correction, having a positive impact on their forecast skills (see [4]–[6]).

Polarimetric ROs (PROs) have been proposed as a complement of the standard ROs for the detection of heavy rain events [7]. The basic concept is that large raindrops, which are often associated with high rain rates, have an asymmetry in their shape: they flatten as they fall. This deviation from sphericity affects the polarization of the GNSS

signal propagation and is expected to be measurable by means of polarimetric differential observables.

The space mission Radio Occultation for Heavy Precipitation with PAZ (ROHP-PAZ), recently launched on February 2018, will obtain polarimetric observables of GNSS-RO thanks to a GNSS polarimetric instrument aboard the low-earth-orbit (LEO) satellite PAZ. The ROHP-PAZ will be a proof-of-concept experiment for GNSS PRO.

In the GNSS PRO technique, the phase shift at L-band induced by heavy rain events is what can be considered as a proxy of the rain rate under certain assumptions. Hence, a PRO event can profile precipitation cells as shown first by Cardellach *et al.* [7]. The precipitation-induced GNSS polarimetric signatures were later confirmed experimentally by Padullés *et al.* [8]. In these ground-based experiments, the observations were not completely explained by the rain alone, and additional effects of ice crystals from high clouds were proposed. This shows that the PRO problem is more complex than originally intended and the vertical profiling of ROs has to be considered to separate the influence of frozen hydrometeors of high tropospheric layers from the rain cells present at lower layers. On the other hand, the ground experiment presented differences respect a GNSS-LEO configuration, such as multipath and lack of troposphere-free crossing rays.

With the next advent of the ROHP-PAZ mission and its differences respect to ground experiments, there is a necessity to characterize the end-to-end propagation of PROs in a GNSS-to-LEO radio-link context. The objective of this paper is to present the necessary conceptual framework to evaluate the separability and the impact of the potential effects in the propagation. This eventually will lead the design of inversion algorithms able to detect and to quantify a vertical profiling of precipitation cells based on the phase-shift retrieval.

In this paper, the theory of PROs is explained based on the end-to-end propagation of the coherent electric field and how its relative polarization gets modified. The identification of the systematic effects on the electric field from both the atmosphere and instrumentation can be summarized as: 1) cells of birefringent media by asymmetric hydrometeors; 2) the circular birefringent medium of the ionosphere; 3) an existing degree of the left-handed component in the GNSS transmission; and 4) an unbalanced polarimetric receiver with variable gain and phase patterns and an initial unknown state.

This paper is organized as follows. Section II describes the propagation case by a briefing on the observation geometry

and the basic definitions and conventions for the electric field and its related observables. Section III summarizes the parameters and the impact of the hydrometeor medium at the L-band propagation, focusing on precipitation. Section IV introduces the ionosphere as the medium after the hydrometeors; the main polarimetric effects on the GNSS transmission are defined and its separability from the hydrometeor ones is shown. Section V deals with realistic transmitter and receiver scenarios for a general propagation case. In Section VI, there is the development of algorithms for the separation of precipitation-related parameters, and finally, in Section VII, such methods are tested under different simulated conditions to assess their validity statistically.

II. STATEMENTS AND DEFINITIONS

In this section, the polarimetric propagation of an RO link is stated, and the fundamental definitions and conventions used through this paper are given.

A. Radio Occultation Geometry

The RO technique relies on the observation of the setting or rising of a satellite by either a ground receiver or an LEO satellite. The studied case in this paper focus on a GNSS-LEO link. The trajectory followed by the transmission is bent by refraction in the atmosphere; after the ionospheric refraction is corrected, the bending angle becomes the basis to measure thermodynamic properties of the neutral atmosphere. GNSS systems use a transmitter antenna in a right-handed (RH) circular polarization (CP), working at L1 and L2 bands, $f_{L1} = 1.575$ GHz and $f_{L2} = 1.227$ GHz (with additionally an L5 frequency designed for the newer generations of GPS at 1.176 GHz).

An RO event consists in a collection of sampled rays in a low grazing angle that profile vertically the atmosphere. The vertical profile is scanned with a variable resolution that depends on the sampling rate and the Fresnel zone [9]; it can vary from 0.1 km near the surface to 1 km at the tropopause. The propagation trajectory of a ray starts at the GNSS satellite and ends at the LEO receiver, having the so-called tangent point as the closest point to the earth center. RO rays are either ordered by its tangent point height h_T or by its time t, existing a nonuniform, one-to-one correspondence between the two which makes them equivalent. One can describe vertical profiles as time series, considering that as the time increases in setting radio occultations, h_T decreases, while in rising ROs, h_T increases.

In Fig. 1, there is a sketch of an RO event. There are two rays to illustrate the possible polarimetric effects while crossing the atmosphere. The high altitude rays cross a long extent of the ionosphere, totally or partially, until they reach the LEO satellite. The same behavior follows for the successive rays, assuming a setting RO, until they reach a tropospheric limit where hydrometeors can be potentially found in the form of precipitation or ice clouds; we set this at $h_t = 20$ km as the tropopause in the tropics. From there downward, the bottom rays cross a section of the ionosphere (ion1) and a section of the troposphere containing possible precipitation cells (tr),
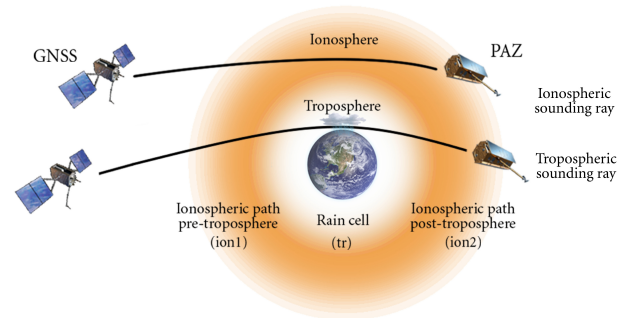

Fig. 1. Schematic of the GNSS-PAZ RO link (not at scale). There are represented two trajectories between a GNSS satellite and the satellite PAZ. The ionospheric sounding ray represents those rays that cross solely a region of the ionosphere (and even a hydrometeor-free troposphere if low enough). The tropospheric-sounding ray represents the bottom rays of the RO which can find precipitation cells along the path. At the bottom of the figure, there are labeled the atmospheric regions crossed by the RO which are potentially able to change the polarization of the transmitted wave.

and cross another section of the ionosphere (ion2) to reach the receiver.

In terms of polarimetric effects, the transmitted CP of the rays above the hydrometeor layer does not experience any change by the Faraday rotation, as it is intended in the design of the GNSS systems. On the other hand, it is expected that the rays that undergo a depolarizing effect by the hydrometeor scattering lose the circularity and, therefore, the rotation effect of the exiting ionosphere path will also affect the propagation until reaching the receiver plane. The polarimetric effects related to the tropospheric propagation will be addressed in Section III, while the addition of the ionosphere will be put in Section IV. Finally, one may introduce nonidealities in the transmitter to consider deviations from the CP from the beginning (Section V).

B. Polarimetric Transmission Equation of the Coherent Field

The propagation can be studied just for the coherent electric field, disregarding the fluctuations of the incoherent field by multiple-scattering effects. This is possible because of the sparse concentration of hydrometeors and to their small scattering cross sections compared with the absorption at frequencies lower than 10 GHz [10]. Hence, we can avoid the Stokes vector and radiative transfer treatment on polarization.

The coherent electric field is modeled by a time-harmonic planar wave, which follows the convention $\mathcal{E}(\boldsymbol{r}, t) = \mathrm{Re}[\boldsymbol{E}e^{j(2\pi ft - kz)}]$, with $\hat{\boldsymbol{z}}$ the direction of propagation [11]. $\boldsymbol{E}$ is a complex vector whose components E_i are phasors for a i-polarization. It is commonly described by using the horizontal and vertical axes $\{\hat{\boldsymbol{h}}, \hat{\boldsymbol{v}}\}$ which form a linear basis in the polarization plane; the vertical axis is contained in the plane of the propagation, while the horizontal axis is perpendicular to it. Alternatively, we can use the circular basis $\{\hat{\boldsymbol{u}}_R, \hat{\boldsymbol{u}}_L\}$ corresponding to circular rotating opposed phasors right and left, so that

$$\boldsymbol{E} = E_h\hat{\boldsymbol{h}} + E_v\hat{\boldsymbol{v}} = E_R\hat{\boldsymbol{u}}_R + E_L\hat{\boldsymbol{u}}_L. \tag{1}$$

The transmission equation of the coherent field can be described in a matrix form. Given an RO trajectory reaching

troposphere as in the low ray of Fig. 1, we have the following equation in the linear basis:

$$\mathbf{E}_r = e^{j\phi_{\mathrm{atm}}} \frac{e^{-jk_0r}}{r} \mathbf{A}\mathbf{T}_{\mathrm{ion2}}\mathbf{T}_{\mathrm{tr}}\mathbf{T}_{\mathrm{ion1}}\mathbf{E}_{\mathrm{in}} \qquad (2)$$

where r is the path of the RO radio link, $\mathbf{A}$ is the receiver polarimetric matrix, which accounts for the gain and phase patterns of the antenna and other instrumental effects of the receiver system, $\mathbf{T}_{\mathrm{ion1}}$ and $\mathbf{T}_{\mathrm{ion2}}$ are the polarimetric transmission matrices for the ionospheric path pretropospher and posttroposphere, respectively, and $\mathbf{T}_{\mathrm{tr}}$ is the polarimetric matrix for the depolarizing scatterers which may be present at the troposphere such as raindrops or ice crystals. $\frac{1}{r}e^{-jk_0r}$ accounts for the free-space propagation phase delay, where k_0 is the free-space propagation constant. An extra phase term ϕ_{atm} is introduced by the atmosphere affecting equally both polarizations, and it is removed in any differential polarimetric observable and it would be any common term in the receiver stage. Finally, $\mathbf{E}_{\mathrm{in}}$ and $\mathbf{E}_r$ are the Jones vectors of the electric field, transmitted and received, respectively.

Looking at (1), the Jones vectors can be defined for linear but also for a circular basis by two different column matrices with the h-v and R-L conventions, respectively

$$\mathbf{E} = \begin{bmatrix} E_h \\ E_v \end{bmatrix} = \begin{bmatrix} E_{0,h} \\ E_{0,v}e^{j\delta} \end{bmatrix} \qquad (3)$$

and

$$\mathbf{E}^c = \begin{bmatrix} E_R \\ E_L \end{bmatrix} = \begin{bmatrix} E_{0,R} \\ E_{0,L}e^{j\delta^c} \end{bmatrix}. \qquad (4)$$

The superindex ^{c} will indicate the circular basis vectors along the text. δ is the polarimetric phase shift between the vertical and horizontal components (analogously, between the left and right components), and $E_{0,i}$ is the amplitude of the i-polarization component.

We use the forward-scattering convention (FSA), meaning that the polarization plane of the wave is seen from the source point of view. Hence, the chirality of the coordinate system follows $\hat{\mathbf{r}} = \hat{\mathbf{v}} \times \hat{\mathbf{h}}$. The sense of rotation follows the IEEE convention, which defines as RH the field whose time evolution at the polarization plane rotates clockwise from the source point of view. Thus, the right-hand sense agrees with the chirality of the FSA convention. This means that $\delta > 0$ corresponds to an RH field and $\delta < 0$ to a left-handed one, conversely for δ^c.

Finally, under the above-described conventions [11], the conversion matrices between the linear and the circular basis are defined as follows:

$$\mathbf{U}_{\mathrm{LC}} = \frac{1}{\sqrt{2}} \begin{bmatrix} 1 & -j \\ 1 & j \end{bmatrix} \qquad (5a)$$

$$\mathbf{U}_{\mathrm{CL}} = \frac{1}{\sqrt{2}} \begin{bmatrix} 1 & 1 \\ j & -j \end{bmatrix}, \qquad (5b)$$

where subindexes LC and CL stand for linear-to-circular and circular-to-linear, respectively.

C. Polarization State Description

A differential polarimetric measurement makes use of the polarization state. There are different ways to work with it, so that a briefing is made here for a coherent wave.

1) Relative Polarization: The polarization state is summarized in the relative polarization factor (also known as polarization ratio), which is the complex ratio of the components of the Jones vector. The definitions used in this paper are the vertical-over-horizontal ratio

$$\chi = \frac{E_v}{E_h} \qquad (6)$$

and the left-over-right ratio

$$\chi^c = \frac{E_L}{E_R}. \qquad (7)$$

The modulus is the (polarimetric) amplitude ratio: $|\chi| = E_{0,v}/E_{0,h}$ and its argument is the polarimetric differential phase $\angle\chi = \delta$. Equivalent polarimetric observables in phase shift and amplitude ratio can be defined for the circular basis.

The relationships between linear and circular relative polarizations using (5a) and (5b) are given by a bilinear transformation that will be often used in this paper

$$\chi^c = \frac{1 + j\chi}{1 - j\chi} \qquad (8a)$$

$$-j\chi = \frac{1 - \chi^c}{1 + \chi^c}. \qquad (8b)$$

2) Elliptic Parameters: It is well known that an ellipse equation can be obtained as the temporal trace of the vector $\mathcal{E}(t, z_0)$. As an alternative to the relative polarization, ellipse-related parameters, namely, the ellipticity ϵ and its orientation angle φ, can be used to describe the polarization state with direct ties with the circular basis description (see a demonstration in [12]).

The ellipticity is the ratio between the major and minor values of the electric field amplitude. It is also related to the amplitudes of $\mathbf{E}^c$

$$\epsilon(\mathrm{dB}) \equiv 20\log\frac{\max|\mathcal{E}|}{\min|\mathcal{E}|} = 20\log\frac{E_{0,R} + E_{0,L}}{E_{0,R} - E_{0,L}} \qquad (9)$$

where for our GNSS propagation case, $E_{0,R} \geq E_{0,L}$ and the absolute value in the ratio definition is dropped. The ellipticity can also be represented by the ellipticity angle $\gamma \in [-(\pi/4), (\pi/4)]$, related as $\tan\gamma = \epsilon^{-1}$.

The orientation angle φ is the angle of the major axis with respect to the horizontal axis counterclockwise, $\varphi \in [-(\pi/2), (\pi/2)]$. The differential phase between L and R components is related to the orientation angle as

$$\delta^c = \delta_L - \delta_R = 2\varphi. \qquad (10)$$

A rotation in the linear basis is equivalent to a phase shift in the circular basis; this convention indicates a negative sign of the orientation if the rotation is RH and positive if left-handed.

III. Polarimetric-RO Propagation in a Hydrometeor Layer

This section summarizes the well-known effects of hydrometeors layers in a wave propagation. The focus is to put on their estimation to determine their significance and separability in a polarimetric measurement at L-band, often overlooked in favor of higher frequencies. We will address the polarimetric phase shift as the main observable related to precipitation and the impact of the differential polarimetric attenuation, also called dichroism.

A. Effective Propagation Medium in Forward Scattering

A layer of hydrometeors acts as an effective medium in terms of propagation of the coherent field. This effect is only possible in the forward-scattering direction due to the coherent sum of the scattered fields coming from every scatterer.

Van de Hulst [13] demonstrated that a propagation through a slab of a sparse distribution of scatterers has an effective complex propagation constant $k_{\mathrm{eff}} = k_0 + k$; k_0 is the free-space propagation constant, while k is the excess term due to the scatterers. The free-propagation term $e^{-jk_0 r}$ will be implicitly carried into the electric field vector, and therefore, our formulation for the transmission matrix only includes the excess propagation term.

The excess propagation constant k is complex and implies both phase shift and attenuation effects per unit length defined in this paper as $k = K - jA$, where K is the specific (or distributed) phase and A is the specific attenuation for the wave amplitude. For a sparse concentration of scatterers, the excess propagation constant approximates as $k = (2\pi/k_0) \int f_{\mathrm{sca}}(D)N(D)\,dD$ [13], where $f_{\mathrm{sca}}(D)$ is the forward-scattering amplitude of a hydrometeor with an equivolumetric diameter D and $N(D)$ is the particle-size distribution.

This approximation can be extended to polarimetry. Those hydrometeors with an oblate shape, namely, raindrops or ice crystal plates, have scattering properties that depend on the polarization component i of the incident wave, $f_{\mathrm{sca},i}$. Thus, the effective propagation medium becomes linearly birefringent because of having different propagation constants along some characteristic axes. The horizontal and vertical axes in the polarization plane are identified as the characteristic axes of the medium when the hydrometeors are considered equally oriented on average, with their symmetry axis aligned with the local zenith by effect of gravity and air dragging. Since the canting angle found for precipitation is often observed and modeled without a preferred orientation (as in absence of wind shear conditions) [14], [15], the h-v axes' identification is a safe assumption.

For polarimetric measurements sensitive to hydrometeors, we are interested in the differential polarimetric parameters (dp). Thus, the differential specific phase is defined by $K_{\mathrm{dp}} = K_h - K_v$ and the differential specific attenuation is $A_{\mathrm{dp}} = A_h - A_v$.

The observables come after an integrated RO propagation, and therefore, the hydrometeor-related parameters to be isolated are the integrated versions of these specific parameters.

Taking the general case of inhomogeneous layers along the RO path L_{tr}, the integrated parameters, namely, the differential phase Φ_{dp} and the differential attenuation τ_{dp}, can be defined as

$$\Phi_{\mathrm{dp}} = \int_{L_{\mathrm{tr}}} K_{\mathrm{dp}}(l)\,dl \tag{11}$$

$$\tau_{\mathrm{dp}} = \int_{L_{\mathrm{tr}}} A_{\mathrm{dp}}(l)\,dl, \tag{12}$$

where it is assumed a variation of the specific parameters along the path due to the particle-size distribution (equivalently the rain rate for precipitation), the type of hydrometeor, and to the angle of incidence.

For every slab of hydrometeor medium, there is a different incidence of the wave, generally oblique; the parallel incidence to the horizon is only attained in the tangent point of the ray. The incidence is determined by both the curvature of the earth which conditions the local orientation of the medium slabs, and by the refractivity gradients which bend the trajectory of the rays. The inclination angle affects the forward-scattering amplitudes and in consequence modifies the propagation constant [16]. In addition, the standard deviations of the individual orientations of the hydrometeors introduce extra factors that decrease the differential propagation constants respect to the vertically oriented distribution [17], [18]. The difference between polarizations removes effects present at both polarizations equally, such as the tropospheric multipath.

Simulations of both the phase shift and the differential attenuation can be carried to estimate the order of magnitude of each integrated parameter. Following the methodology of Cardellach et al. [19], trajectories of actual Constellation Observing System for Meteorology, Ionosphere, and Climate (COSMIC) radio occultations colocated with precipitation information by the Tropical Rainfall Measuring Mission (TRMM) and Global Precipitation Measurement (GPM) satellites were calculated for the integration, including a constant standard deviation of the canting angle of 5°. The ray-tracing method (see [20]) applied here has only considered the atmospheric refraction, avoiding effects of diffraction or multipath as explained earlier as they do not alter the polarimetric observable; a 5° constant standard deviation of the canting angle was modeled for the raindrops.

The polarimetric phase shift is the main observable sensitive to the precipitation content. Fig. 2 shows the histogram of the equivalent delay in mm of the phase shift by precipitation, $(\lambda/2\pi)\Phi_{\mathrm{dp}}(f)$. The equivalent delay is practically invariant for the frequencies used in GNSS for all possible rain rates available. The histogram gathers for every ray those precipitation events colocated with COSMIC RO from 2006 to 2014 that would have been potentially measured. Looking at it, we can establish an upper limit of 20 mm as the maximum registered case. For L1, this corresponds to a phase shift of $\sim$39°; the equivalent limits would be 29.6° and 29° for L2 and L5, respectively. Cardellach et al. [19] assumed that the ROHP-PAZ experiment noise level for Φ_{dp} would be $\sim$1.5 mm at the bottom layers of the troposphere, being this a conservative figure: in [7], it was shown that at higher altitudes, the noise limits are lower. Therefore, following the
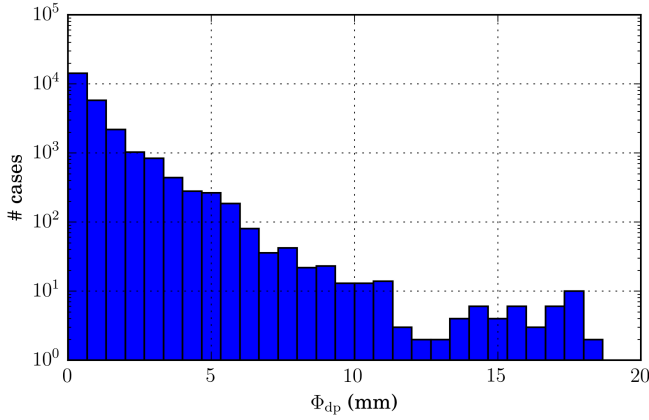
Fig. 2. Distribution of the polarimetric delay in mm induced by precipitation from a database of 30 000 cases of RO trajectories with precipitation content, from a set of 550 RO events.

same limits, we will assume henceforth that measurements of $\Phi_{\rm dp}$ <1.5 mm would be under the noise level as the most restrictive situation. The effect on the GNSS propagation will be studied in Section III-B.

As a rule of thumb (see [14]), the differential attenuation becomes significant from 5 GHz onward. For that reason, the attenuation at L-band is often overlooked in the literature. Our simulations of forward scattering at L-band (by the T-matrix method) shows that the order of magnitude of the differential specific attenuation $A_{\rm dp}$ is found between 10^{-3} and 10^{-5} dB/km (depending on the drop-size distribution considered) with a maximum expected differential attenuation around $\tau_{\rm dp}$ =0.02 dB, corresponding to very high rain rate scenarios. Although having a minor role, its effect will be analyzed in Section III-C.

B. Change of Polarization on a Circular Wave at L-Band: Phase Shift

As shown in Section III-A, the detection of polarimetric properties at L-band is mainly sensitive to the phase shift rather than the dichroism. A sensible approximation is to assume that the dichroism is negligible and the transmission matrix belongs to a case of pure polarimetric phase shift. So that in the above-stated linear basis,

$$\mathbf{T}_{\rm tr} \approx \begin{bmatrix} e^{-j\Phi_h} & 0 \\ 0 & e^{-j\Phi_v} \end{bmatrix}. \tag{13}$$

It is straightforward to see that for a depolarizing layer, the output differential phase $\phi_{\rm tr} = \angle\chi_{\rm tr}$ is the sum of the initial differential phase and the induced polarimetric phase shift $\Phi_{\rm dp} = \Phi_h - \Phi_v$, provided both ideal transmission and reception. For the right handed circular polarization (RHCP) input $\mathbf{E}_{\rm in} = (E_{0,\rm RHCP}/\sqrt{2})[1 \quad j]^T$, we get

$$\phi_{\rm tr} = \frac{\pi}{2} + \Phi_{\rm dp}. \tag{14}$$

However, the alternative circular basis representation becomes useful as other potential effects are taken into account as we will see along the text. For this case, we have the transmission matrix formulated as $\mathbf{T}_{\rm tr}^c = \mathbf{U}_{\rm LC}\mathbf{T}_{\rm tr}\mathbf{U}_{\rm CL}$, which

for the noncanted hydrometeors becomes

$$\mathbf{T}_{\rm tr}^c = \frac{1}{2}\begin{bmatrix} T_{\rm hh} + T_{\rm vv} & T_{\rm hh} - T_{\rm vv} \\ T_{\rm hh} - T_{\rm vv} & T_{\rm hh} + T_{\rm vv} \end{bmatrix}. \tag{15}$$

For the transmission matrix, we can define the crosspolar-to-copolar circular ratio p, which is the circular relative polarization output for an RHCP input

$$p = \chi_{\rm tr}^c\big|_{\rm RHCP} = \frac{T_{\rm hh} - T_{\rm vv}}{T_{\rm hh} + T_{\rm vv}}. \tag{16}$$

Then, for an RHCP field, the output circular relative polarization under negligible dichroism is

$$p|_{A_{\rm dp}=0} = \frac{1 - e^{-j\Phi_{\rm dp}}}{1 + e^{-j\Phi_{\rm dp}}} = -j\tan\frac{\Phi_{\rm dp}}{2}. \tag{17}$$

For a pure RHCP input wave after a pure phase shift layer, the output polarization becomes elliptic. From the argument of (17) and the definition of the orientation angle (10), one can see that the ellipse is rotated $\varphi = -(\pi/4)$ (thus, RH) independently of $\Phi_{\rm dp}$. The phase-shift value only affects the ellipticity of the field, slightly flattening its roundness across the first-quadrant bisectrix direction.

The flattening is seen in the ellipticity angle γ, which can be obtained by the following expression using the result in (17):

$$\tan\gamma = \frac{1 - \tan\frac{\Phi_{\rm dp}}{2}}{1 + \tan\frac{\Phi_{\rm dp}}{2}} = \frac{\tan\frac{\pi}{4} - \tan\frac{\Phi_{\rm dp}}{2}}{1 + \tan\frac{\pi}{4}\tan\frac{\Phi_{\rm dp}}{2}}$$
$$= \tan\left(\frac{\pi}{4} - \frac{\Phi_{\rm dp}}{2}\right). \tag{18}$$

If we set as an upper boundary $\Phi_{\rm dp} = 38.7°$ (equivalent to 20 mm), the maximum possible flattening is of an ellipticity angle of 35°, a 10° deviation from roundness.

The ellipticity as the inverse of $\tan\gamma$ after some manipulations is given in dB by the form

$$\epsilon(\rm dB) = 20\log\left[\tan\left(\frac{\Phi_{\rm dp}}{2} + \frac{\pi}{4}\right)\right] \approx 0.292\Phi_{\rm dp}(\rm mm) \tag{19}$$

where the second approximation is valid for all possible values at L1-band.

C. Change of Polarization on a Circular Wave at L-Band: Differential Attenuation

Respect to the previous section, now we study the impact of the dichroism of the precipitation medium as a minor term affecting both the orientation and ellipticity of the polarization ellipse. We focus particularly in the raindrop dichroism, because the dichroism by ice particles can be assumed as negligible at L-band due to even more smaller values of integrated attenuation.

We start defining the linear copolar ratio as an auxiliary term, where not only the polarimetric phase shift $\Phi_{\rm dp}$ is present but also the differential attenuation $\tau_{\rm dp}$ from (12):

$$g = \frac{T_{\rm vv}}{T_{\rm hh}} = e^{\tau_{\rm dp}+j\Phi_{\rm dp}} \tag{20}$$

whose module has a value close to 1.

When considering oblate raindrops, from L-band onward, the differential attenuation is always positive $\tau_{\rm dp} > 0$ because

of the larger attenuation experienced at the horizontal polarization with respect to the vertical one; therefore, $|g| > 1$. The effect of $|g| \neq 1$ on the elliptic field is best seen using the circular basis. In this case, the circular relative polarization for an RHCP input defined previously (17) now becomes using (20)

$$p(g) = \frac{1-g}{1+g} = \frac{1-|g|^2 - j2\,\mathrm{Im}[g]}{|1+g|^2} \tag{21}$$

having its argument as

$$\angle p = \arctan \frac{2|g| \sin \Phi_{\mathrm{dp}}}{|g|^2 - 1}$$
$$\approx -\frac{\pi}{2} - \frac{e^{2\tau_{\mathrm{dp}}} - 1}{2e^{\tau_{\mathrm{dp}}} \sin \Phi_{\mathrm{dp}}} \tag{22}$$

assymptotically approximated because $|g| \gtrsim 1$.

Thus, the orientation angle of the elliptic field is deviated RH by an additional $\Delta\varphi$ angle-dependent on both τ_{dp} and Φ_{dp} ($\Phi_{\mathrm{dp}} \neq 0$)

$$\Delta\varphi(\tau_{\mathrm{dp}}, \Phi_{\mathrm{dp}}) = -\frac{e^{2\tau_{\mathrm{dp}}} - 1}{4e^{\tau_{\mathrm{dp}}} \sin \Phi_{\mathrm{dp}}}. \tag{23}$$

This extra rotation can be interpreted as the larger attenuation on the horizontal axis stretching the ellipse, which makes that the diagonally oriented ellipse rotates further in the RH sense.

On the other hand, given a certain Φ_{dp}, the variation caused by τ_{dp} in the modulus of p can be assessed using a first-order approximation of $p(g) = p(|g|)$ around $|g| = 1$ (equivalent to approximate around $\tau_{\mathrm{dp}} = 0$) with the auxiliary term $p_0 = \tan(\Phi_{\mathrm{dp}}/2)$

$$p(|g|) \approx p(1) + (|g| - 1) \left. \frac{dp}{d|g|} \right|_{|g|=1}$$
$$= -j|p_0| + (|g| - 1)\left[j|p_0| + \frac{1}{2}(1 - |p_0|^2) \right] \tag{24}$$

and the modulus for this expression results

$$|p(\tau_{\mathrm{dp}}, \Phi_{\mathrm{dp}})| = |-jp_0 + (e^{\tau_{\mathrm{dp}}} - 1)\left[jp_0 + \frac{1}{2}(1 - p_0^2) \right]|$$
$$= \left| \frac{1}{2}(e^{\tau_{\mathrm{dp}}} - 1)(1 - p_0^2) + j(e^{\tau_{\mathrm{dp}}} - 2)p_0 \right| \tag{25}$$
$$\approx \frac{1}{2}\sqrt{\tau_{\mathrm{dp}}^2 + \Phi_{\mathrm{dp}}^2} \tag{26}$$

where for the last approximation, we have used $\exp(\tau_{\mathrm{dp}}) \approx 1 + \tau_{\mathrm{dp}}$ and $\tan(\Phi_{\mathrm{dp}}/2) \approx \Phi_{\mathrm{dp}}/2$.

Equations (23) and (25) can be evaluated using the statistics about Φ_{dp} and τ_{dp} obtained in the simulations that used the COSMIC-TRMM (or -GPM) collocations (as in Fig. 2). Both parameters are related according to microphysical rain parameters and the path length. Fig. 3 (top) shows the relative deviation of the modulus of p from the no-dichroism case. The relative error assumed if the attenuation is not considered is not larger than 0.5%. Fig. 3 (bottom) shows the extra orientation angle $\Delta\varphi$ where it is shown that it cannot be larger than 0.2°. Therefore, we can conclude that the impact of the differential attenuation is negligible compared with the phase shift, and it will be safely skipped hereafter.
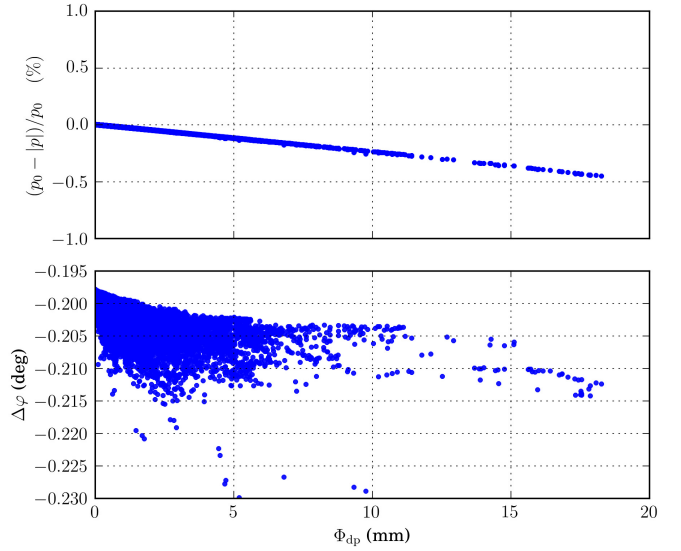

Fig. 3. Effects of the raindrop differential attenuation in the change of polarization at the L-band circularly polarized signals both in amplitude and phase as a function of the rain-induced polarimetric phase shift in mm. (Top) Relative error in the modulus of p. (Bottom) Orientation departure of the polarization ellipse.

IV. POLARIMETRIC PROPAGATION IN THE IONOSPHERE

A. Ionospheric Effects on Polarization

The ionosphere is a magnetoionic dispersive medium where the earth's magnetic field and cold plasma interact varying in space and time. Under some simplifications, the ionosphere induces two characteristic propagation modes that in general are elliptic polarizations with the opposite rotation senses [21]. As ellipses, the modes can be considered as a mixed case of a linear polarization and a CP. One can assign respective differential propagation constants on linear polarization and CP, where each one depends on a different component of the magnetic field $\boldsymbol{B}$ with respect to the wave propagation direction $\hat{\mathbf{r}}$.

On one hand, for the linear differential polarization, there is a phase shift by linear birefringence which comes as a function of the transversal component B_T (orthogonal to the propagation); this is called the Cotton–Mouton effect. On the other hand, the Faraday rotation effect rotates the polarization ellipse by circular birefringence, which depends on the longitudinal component of the magnetic field $B_L = \boldsymbol{B} \cdot \hat{\mathbf{r}}$; the rotation is RH if the component is parallel and left-handed if antiparallel.

The Cotton–Mouton phase shift is lower than the Faraday rotation due to a different frequential dependence. Thus, for frequencies of the order of hundreds of MHz and above (as in radiofrequencies), the polarization changes are just of rotation due to the longitudinal component and valid for practically all alignments of the magnetic field with the propagation direction (quasi-longitudinal approximation) as demonstrated by Yeh et al. [22].

Under the quasi-longitudinal approximation, the Faraday rotation at an RO-trajectory position r is given by

$$\Omega(r) = -\frac{2.36 \cdot 10^4}{f^2} \int N_e(r) B_L(r)\, dr \tag{27}$$

where the constant is for SI units, N_e is the density of electrons/m^3, and B_L is the longitudinal magnetic field. The opposite sign gives the convention of an RH rotation for a longitudinal component parallel to the propagation direction.

From the linear basis point of view, it is shown that the circular birefringence corresponds to a rotation transformation of the polarization ellipse. For each differential path dr, there is a rotation matrix such as

$$\mathbf{R}(d\Omega) = \begin{bmatrix} \cos d\Omega & -\sin d\Omega \\ \sin d\Omega & \cos d\Omega \end{bmatrix}. \tag{28}$$

The net rotation with the integrated angle can be assumed as the chained product of rotation matrices: $\mathbf{R}(\Omega) = \mathbf{R}(\int d\Omega) = \prod_i \mathbf{R}_i(d\Omega)$.

The rotation effect can only be experienced by a noncircular field, such as the output from a precipitation layer. Notice that in the case of CP $\mathbf{E}_{CP} = [1 \quad \pm j]^T$, the rotated field gets a common phase at both components $\mathbf{E}_{out} = \mathbf{R}(\Omega)\mathbf{E}_{CP} = e^{j\Omega}\mathbf{E}_{CP}$ so that its polarization state does not change and remains circular, $\chi_{out} = \chi_{CP} = \pm j$.

An ionospheric-rotated field $\mathbf{E}_{out} = \mathbf{R}(\Omega)\mathbf{E}_{in}$ if expressed in a circular base as $\mathbf{U}_{LC}\mathbf{E}_{out}$ shows the rotation as a phase shift between the left and right components. The relative polarization output is

$$\chi_{out}^c(\Omega) = e^{j2\Omega}\chi_{in}^c. \tag{29}$$

We can see that the ionospheric transmission matrix in the L-band as a *circular* birefringent medium, being the dual case compared with the hydrometeor transmission matrix in (13). The ionospheric-induced circular phase shift is twice the Faraday rotation angle, $\Phi_L - \Phi_R = 2\Omega$, where $\Phi_{R,L}$ is the excess phase terms for the CPs.

B. Estimation of Faraday Rotation Values

While for higher frequencies, the Faraday rotation is a small effect, at L-band, it is a meaningful polarimetric effect when the polarization is not completely circular, as expected to be after the change of polarization state by hydrometeors.

As a way to characterize the distribution and maximum values for the rotation angle in ROs, numerical simulations of (27) have been made. As previously stated, they have been applied on real RO trajectories from the COSMIC mission colocated with actual precipitation TRMM observations during the 2006–2014 period for a total of 550 fully simulated events. The ionospheric acquisition mode (not present for every RO) provides around 200 rays, at one second rate, corresponding to tangent point altitudes between 450 and 130 km height. The tropospheric RO rays are taken below 130 km each 20 ms during 120 s approximately for an amount of ~6000 rays.

The profiles of both electron density and earth's magnetic field at each point of the trajectories have been set to the IRI-2012 model (the International Reference Ionosphere) [23] and the IGRF-12 model (the International Geomagnetic Reference Model) [24], respectively. They are defined for a height interval from 100 to 600 km as an intersection, where both factors are meaningful to their contribution in the integral; below 100 km, the electron density content is five orders of magnitude lower than the peak value, and above 600 km,
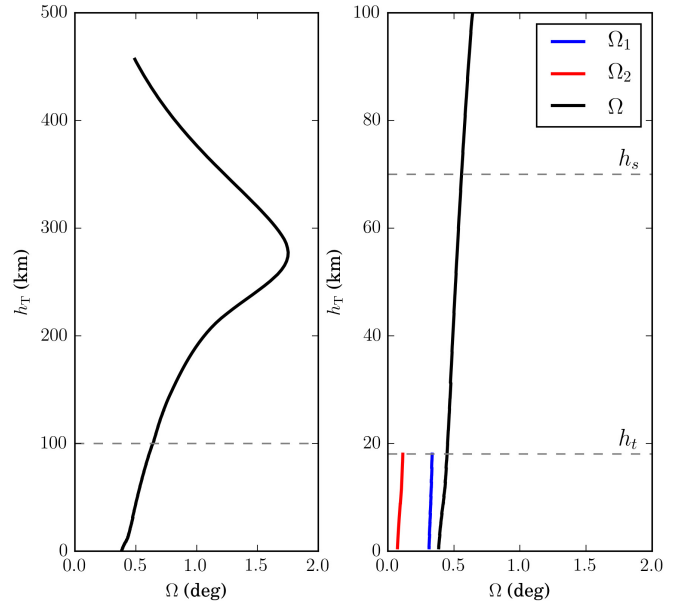

Fig. 4. Simulated vertical profile of the Faraday rotation angle for the COSMIC RO ID:C001.2006.233.17.15.G28, exemplifying the behavior of the angle in ROs. (Left) Profile showing the expected variation of Ω for integrated RO trajectories, which is partially tracing the ionospheric layer. (Right) Zoomed-in view of the latest 100 km where the smooth variation of the profile is found. The angle has been splitted in its pretroposphere and posttroposphere contributions after the troposphere boundary where hydrometeors are potentially found. The horizontal dashed lines show a possible height interval where the linear behavior of Ω is granted for calibration purposes.

both magnetic field and electron density decrease quickly, but higher than the PAZ orbit, which is expected at 514 km, ensuring that there is no meaningful gap in the modeled integration toward the receiver.

These models account for monthly averaged properties, and thus, this paper aims to quiet to moderate geomagnetic and ionospheric conditions, while extreme episodes may become underestimated and the statistics smoothed. Nonetheless, high values of the ionosphere properties do not necessarily imply a high net rotation value, since there may be partial cancellations because of opposite alignments of the magnetic field along the integrated path, a possible circumstance in a sat-to-sat limb sounding.

1) Vertical Profile of the Rotation Angle: As shown in Fig. 1, the vertical profile of the rotation angle affecting the propagation can be split in two different regions, as shown by the simulation in Fig. 4. The top region, where the layers of the ionosphere are crossed tangentially and their vertical structure is partially traced because the rays sweep across its gradient. The bottom region, where the contributions of the $N_e B_L$ product to (27) integral become smaller and the difference between consecutive rays decrease to be almost constant, showing a smoothiness in the profile. This is indicated by the height boundary h_s (assuming height as that of the RO tangent point).

Rays with tangent point heights below h_s sweep a similar section of the ionosphere, because their incidence angles are close to the gradient of the ionospheric variation. In addition, this region is separated by the tropospheric boundary
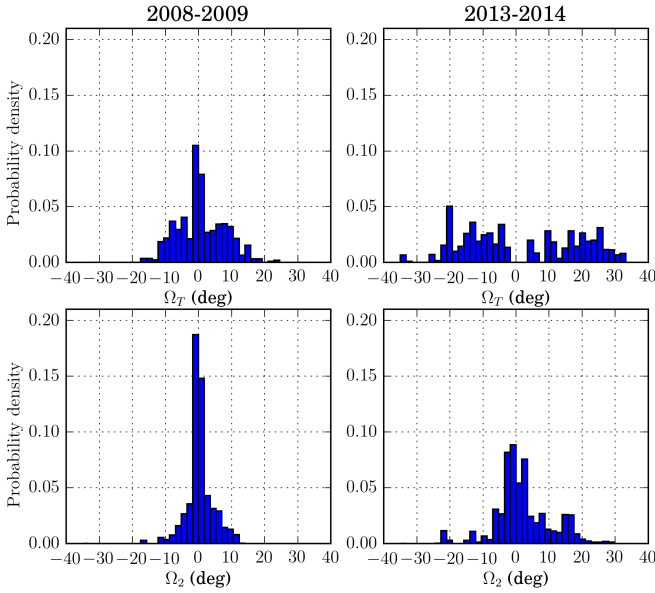
Fig. 5. Histograms of the (Top row) total rotation angle and the (Bottom row) posttroposphere rotation angle for the trajectories below $h_t = 20$ km, for a total of 220 000 cases. For comparison, there are the (Left column) minimum solar activity period (2008–2009) and the (Right column) maximum solar activity period (2013–2014), respectively. The slight bias toward positive values noticeable in Ω_2 can be explained by the major number of accounted RO cases in the northern hemisphere, where many of them have a relative alignment with the magnetic field that gives a positive net rotation for the posttroposphere region.

set at h_t. Since precipitation and other hydrometeors might occur below h_t, one has to make a distinction between the pretroposphere angle Ω_1 and the posttroposphere angle Ω_2, as modeled by the transmission equation of (2) (see also Fig. 1). To summarize, we define three regions based on the altitude of the tangent point: above h_s where the rotation angle Ω behaves nonlinearly in altitude; below h_s, where it does; and below h_t, where the different ionospheric effects might happen (before and after crossing the hydrometeors).

2) Statistics of the Rotation Angle: The statistics of Ω are carried over the set of simulated RO rays below h_t for a total of 220 000 trajectories. Fig. 5 shows a histogram of Ω at the L1-band for a period of minimum solar activity (2008–2009) and a period of maximum solar activity (2013–2014). One can see that the distribution is almost symmetrical centered at zero, being broader for the maximum activity in the ionosphere.

As the worst case, we can set a boundary for the rotation angle of $\pm 30°$. The equivalent values at frequency bands L2 and L5 would be $\pm 49°$ and $\pm 53°$, respectively.

The posttroposphere ionospheric path is responsible for a rotation Ω_2 in a field whose ellipticity has been induced by the presence of tropospheric hydrometeors. Therefore, its statistics are specifically needed to deal with the retrieval of the precipitation. In Fig. 5, they are shown for $h_T \leq h_s$. The values can be restricted to an interval of $\pm 15°$ at L1, equivalent to $\pm 24°$ (L2) and $\pm 26.9°$ (L5).

C. Separability of Ionospheric Rotation From Hydrometeor Phase Shift

1) Circular Basis Representation: The noncircular field found after crossing hydrometeors is rotated by the ionosphere

present in the path between the troposphere and the LEO satellite by a matrix $\mathbf{T}_{\text{ion2}} = \mathbf{R}(\Omega_2)$. The standard approach for a polarimetric measurement is to measure both amplitude and phase. Then, we can separate the effects of phase shift and rotation when it is formulated in a circular basis because of the circular phase factor that models the rotation effect in (29).

Given the pure phase shift approximation in the L-band for $\mathbf{T}_{\text{tr}}$ and the received field as $\mathbf{E}_{\text{ion}} = \mathbf{T}_{\text{ion2}}\mathbf{T}_{\text{tr}}\mathbf{E}_{\text{RHCP}}$, the circular relative polarization output after crossing ion2, using (17), is

$$\chi^c_{\text{ion2}} = p e^{j2\Omega_2} = -j e^{j2\Omega_2} \tan \frac{\Phi_{\text{dp}}}{2}. \tag{30}$$

The precipitation phase-shift effect Φ_{dp} is only present in the amplitude ratio as in (17), while the Faraday rotation angle posttroposphere Ω_2 is only present in the circular differential phase, with no influence of one to the other

$$\angle \chi^c_{\text{ion2}} = -\frac{\pi}{2} + 2\Omega_2. \tag{31}$$

Therefore, a full-polarimetric measurement is enough to estimate both effects, precipitation and ionosphere.

2) Linear Basis Representation: Whereas a full-polarimetric measurement of the electric field theoretically allows the separability of Φ_{dp}, this feature cannot be granted due to low SNR scenarios in ROs for the lowest rays (see [7]), fading events and the difficulties of a proper amplitude calibration. Hence, an alternative approach based on the linear differential phase $\angle \chi_{\text{ion2}}$ is developed (note that in the previous section, the circular differential phase $\angle \chi^c_{\text{ion2}}$ was used instead). This is the base for the phase-polarimetric retrieval explained in this paper.

After the posttroposphere rotation, we can use the relation between relative polarizations (8b) to get

$$-j\chi_{\text{ion2}} = \frac{1 - p e^{j2\Omega_2}}{1 + p e^{j2\Omega_2}} = \frac{1 - |p|^2 - j2\,\text{Im}[p e^{j2\Omega_2}]}{|1 + p e^{j2\Omega_2}|^2}. \tag{32}$$

Considering the case of zero-mean canting angle with no dichroism, $p = -j\tan(\Phi_{\text{dp}}/2)$ is replaced

$$-j\chi_{\text{ion2}} = \frac{1 - \tan^2 \frac{\Phi_{\text{dp}}}{2} + j2 \tan \frac{\Phi_{\text{dp}}}{2} \cos 2\Omega_2}{|1 + p e^{j2\Omega_2}|^2}. \tag{33}$$

Finally, the differential phase as the argument of χ_{ion2} is

$$
\begin{aligned}
\angle \chi_{\text{ion2}} &= \frac{\pi}{2} + \arctan\left(\cos 2\Omega_2 \frac{2 \tan \frac{\Phi_{\text{dp}}}{2}}{1 - \tan^2 \frac{\Phi_{\text{dp}}}{2}} \right) \\
&= \frac{\pi}{2} + \arctan(\cos 2\Omega_2 \tan \Phi_{\text{dp}}).
\end{aligned}
\tag{34}
$$

In the absence of ionosphere, the differential phase would be the result seen previously in (14). As seen in Section IV-B, Ω_2 is expected to be distributed symmetrically between $\pm 15°$; then, the $\cos 2\Omega_2$ factor may reach a value of 0.86 as the worst case of ionospheric peak activity.

With the expected values for both Ω_2 and Φ_{dp}, the arctangent can get linearized by its argument for a wide range of values, losing accuracy as either one of them exceeds the condition of the small angle (this will be further discussed in Section VI-B1).

The approximation of the arctangent and the two respective additional small-argument approximations for the rotation and the phase shift define a linear approximation for the postionosphere differential phase

$$\angle \chi_{\text{ion2}} \approx \frac{\pi}{2} + \left(1 - 2\Omega_2^2\right)\Phi_{\text{dp}}, \tag{35}$$

where $\tan \Phi_{\text{dp}} \approx \Phi_{\text{dp}}$ and $\cos 2\Omega_2 \approx 1 - 2\Omega_2^2$ have been used. Equation (35) would correspond to the GNSS PRO differential phase measurement if the transmitted wave was perfectly circular and the receiver did not induce any further effects.

V. REALISTIC POLARIMETRIC-RO PROPAGATION: TRANSMITTER AND RECEIVER EFFECTS

This section deals with nonidealities at the both ends of the transmission equation. They alter the results seen so far in the previous sections, and the propagation is now fully modeled according to (2).

A. Receiver Effects

The GNSS polarimetric receiver has two kinds of instrumental systematic effects: 1) a fixed one based on the receiver architecture and 2) a variable one dependent on its initial state for each RO measurement. The receiver matrix can be seen as a product between a phase shift matrix and a gain matrix

$$\mathbf{A} = \begin{bmatrix} 1 & 0 \\ 0 & e^{j\phi_{\text{arc}}} \end{bmatrix} \begin{bmatrix} a_{\text{hh}} & a_{\text{hv}} \\ a_{\text{vh}} & a_{\text{vv}} \end{bmatrix}. \tag{36}$$

The left matrix models the unknown initial phase shift of the GNSS receiver. The right matrix is the gain and the phase pattern matrix for the antenna ports, where copolar coefficients are dependent on the angle of arrival of the ray, according to the antenna pattern $a_{ii}(\theta_r, \phi_r)$; the crosstalk between the channels is modeled by the complex coefficients a_{ij}, $a_{\text{hv}} \neq a_{\text{vh}}$.

The received components h and v contain a cross-polarization element due to a_{ij} coefficients

$$E_{h,r} = a_{\text{hh}}E_{h,\text{in}} + a_{\text{hv}}E_{v,\text{in}} = E_{h,\text{cp}} + E_{h,\text{xp}} \tag{37a}$$
$$E_{v,r} = a_{\text{vv}}E_{v,\text{in}} + a_{\text{vh}}E_{h,\text{in}} = E_{v,\text{cp}} + E_{v,\text{xp}}. \tag{37b}$$

The first terms are the copolar ones, $E_{i,\text{cp}}$, while the second terms are the cross-polar $E_{i,\text{xp}}$.

The cross-polar isolation is defined as the ratio between copolar and crosspolar powers received at a given port i

$$\text{XPI}_i = 20\log\left|\frac{E_{i,\text{cp}}}{E_{i,\text{xp}}}\right| = 20\log\left|\frac{a_{ii}}{a_{ij}}\right| \quad i = \text{h}, \text{v} \tag{38}$$

assuming the same power input at h and v to test the system.

The isolation achieved in the PAZ receiver antenna is on the order of 30 dB at L1 ($\sim$27 dB at L2) making $|a_{ij}| \ll |a_{ii}|$. Under this assumption, the receiver matrix that we consider henceforth is approximated as

$$\mathbf{A} \approx \begin{bmatrix} a_{\text{hh}} & 0 \\ 0 & a_{\text{vv}}e^{j\phi_{\text{arc}}} \end{bmatrix}. \tag{39}$$

TABLE I
MAXIMUM ADMITTED ELLIPTICITIES IN GPS

Band	Block IIA[*]	Block IIR/IIR-M/IIF/GPS III
L1	<1.2 dB	<1.8 dB
L2	<3.2 dB	<2.2 dB
L5	not applicable	<2.4 dB[**]

[*]Decommissioned on 25 Jan. 2016

[**]Available for all block IIF and beyond

B. Elliptic Transmission

The specifications of GNSS give a tolerance for the ellipticity (as axial ratio) of the transmission beyond a CP. For the GPS satellites, several values are given as a function of frequency and satellite generation, as seen in Table I composed according to [25] and [26] for maximum ellipticities over the angular range of $\pm 13.8°$ from nadir.

This relaxed constraint on the circularity models the initial transmitted field as

$$\mathbf{E}_{\text{in}}^c = E_{R,\text{in}} \begin{bmatrix} 1 \\ me^{j\Delta} \end{bmatrix} \tag{40}$$

where m is the initial amplitude ratio of the transmitted field $m = |E_L|/|E_R|$ and Δ is the initial circular phase shift $\Delta = \delta_L - \delta_R$, related with the initial orientation of the transmitted field [see (10)]. Δ is completely undetermined and can have any value between $\pm\pi$, while the worst m is conditioned to the worst ellipticity in Table I by

$$m = \frac{\epsilon - 1}{\epsilon + 1}. \tag{41}$$

We assume that for the complete RO event, the ellipticity degree does not change appreciably along the height, but each satellite potentially has a different value. If we compare the worst case scenario transmitted ellipticities to the ellipticity induced by hydrometeors, described by (19), we can see that the latter is comparable below a certain value of phase shifts. This result makes relevant to assume a nonideality in the transmission. Hence, a study is necessary to estimate the impact of the parameter and to design a procedure to remove as much as possible the influence of the nondesired ellipticity sources from the one that is related to the precipitation. As explained in Section V-C, the initial ellipticity is responsible to the further mixing of atmospheric and ionospheric effects, which adds an extra complexity compared with the ideal case of Section IV-C which needs to be assessed.

C. General Polarimetric Propagation Case

Considering all the above-described effects, the resulting received field has a more complex formulation. Recalling the transmission equation, the most general case we have considered so far is

$$\mathbf{E}_r = \mathbf{A}\left(\frac{a_{\text{vv}}}{a_{\text{hh}}}, \phi_{\text{arc}}\right)\mathbf{R}(\Omega_2)\mathbf{T}_{\text{tr}}(\Phi_{\text{dp}})\mathbf{R}(\Omega_1)\mathbf{E}_{\text{in}}(m, \Delta) \tag{42}$$

for low RO rays. $\Omega_{1,2}$ are the Faraday rotation angles for the ionospheric paths of pretroposphere and posttroposphere,

respectively. The tropospheric transmission matrix contains a term of phase shift and a term of dichroism.

We can develop step by step the relative polarization factor after each matrix. First, the initial elliptic field is rotated after the ionospheric path pretroposphere until reaching the troposphere

$$\chi_{\text{ion1}}^c = me^{j(\Delta + 2\Omega_1)}. \tag{43}$$

The rotated field now is affected by the hydrometeor layers. Since the input field is not circularly polarized, it is useful to compare the RHCP input situation described previously with the current one. Thus,

$$
\mathbf{E}_{\text{tr}}^c = \frac{E_{R,\text{in}}}{2} \begin{bmatrix} T_{\text{hh}} + T_{\text{vv}} & \chi_{\text{in}}^c(T_{\text{hh}} - T_{\text{vv}}) \\ T_{\text{hh}} - T_{\text{vv}} & \chi_{\text{in}}^c(T_{\text{hh}} + T_{\text{vv}}) \end{bmatrix}
$$
$$
= E_{R,\text{in}} \frac{T_{\text{hh}} + T_{\text{vv}}}{2} \begin{bmatrix} 1 + p\chi_{\text{in}}^c \\ p + \chi_{\text{in}}^c \end{bmatrix} \tag{44}
$$

where the definition for p is given by (16) and may include all the effects of dichroism and canting together with the phase shift. Equation (45) gives the tropospheric-output relative polarization factor. Replacing terms for χ_{in}^c with those for the current case, we have

$$\chi_{\text{tr}}^c = \frac{p + me^{j(\Delta + 2\Omega_1)}}{1 + pme^{j(\Delta + 2\Omega_1)}}. \tag{45}$$

After the troposphere, the ionosphere posthydrometeor introduces another rotation factor $e^{j2\Omega_2}$. Therefore,

$$\chi_{\text{ion2}}^c = e^{j2\Omega_2} \frac{p + me^{j(\Delta + 2\Omega_1)}}{1 + pme^{j(\Delta + 2\Omega_1)}} \tag{46}$$

is the relative polarization that reaches the antenna plane.

Finally, the receiver matrix gives the received linear relative polarization. Considering the approximation by perfect isolation of the channels by (39), we get

$$\chi_r = \frac{a_{\text{vv}}}{a_{\text{hh}}} e^{j\phi_{\text{arc}}} \chi_{\text{ion2}} = \frac{a_{\text{vv}}}{a_{\text{hh}}} e^{j\phi_{\text{arc}}} j \frac{1 - \chi_{\text{ion2}}^c}{1 + \chi_{\text{ion2}}^c} \tag{47}$$

recalling the bilinear relation in (8a).

An important assumption that we can do is a linear approximation on (46). As seen from the Section III-C and Section V-B, $p < 1$ and $m < 1$ imply $|mp| \ll 1$, which lead to

$$\chi_{\text{ion2}}^c \approx pe^{j2\Omega_2} + me^{j\theta} \tag{48}$$

where $\theta = \Delta + 2\Omega_1 + 2\Omega_2$ is the auxiliary angle.

The circular relative polarization at the antenna plane is the sum of two factors: one due to the polarization by hydrometeors through the exiting ionosphere, $pe^{j2\Omega_2}$, and the second due to the initial transmitted polarization through the entire ionosphere, $me^{j\theta}$. The maximum value of $|p|$ is around 0.33, which is comparable to the maximum values for m; thus, both components are equally meaningful. We can reformulate the observed relative polarization as

$$\chi_r = \frac{a_{\text{vv}}}{a_{\text{hh}}} e^{j\phi_{\text{arc}}} j \frac{1 - pe^{j2\Omega_2} - me^{j\theta}}{1 + pe^{j2\Omega_2} + me^{j\theta}}. \tag{49}$$

The concurrence of several systematic effects and the way how they mix makes difficult the retrieval of the hydrometeor-induced effect p from the rest in comparison with Section IV-C. The separability of the parameters and the suggested procedures to achieve it is discussed in Section VI.

VI. SEPARATION ALGORITHMS

A. Observable and Calibrated Phase

The GNSS receiver design relies on the accuracy of phase measurements, while the tropospheric RO rays are expected to have a low SNR. Hence, a full-polarimetric method measuring both amplitudes and phases in the troposphere is not considered suitable for every RO case. However, under several approximations, it is possible to separate the hydrometeor phase shift Φ_{dp} from the rest of terms (transmitter, receiver, and ionospheric effects). The separation algorithms are based on the linear phase approach seen in (35) and develop from the expression in (49).

The measurements along the region are given by the observables $E_{h,\text{obs}}(t)$ and $E_{v,\text{obs}}(t)$, where from now on, the time series will be explicitly shown. We will assume a setting RO, but a rising RO only needs to redefine the order of some time intervals defined in the following. We define the observed differential phase as

$$\phi_{\text{obs}} = \angle E_{v,\text{obs}} - \angle E_{h,\text{obs}} \tag{50}$$

which we identify as the estimate of the argument of the relative polarization at the receiver plane: $\phi_{\text{obs}} = \angle \hat{\chi}_r(t)$ and the following phase equation can be set:

$$\phi_{\text{obs}}(t) = \phi_{\text{ant}}(t) + \phi_{\text{arc}} + \angle \chi_{\text{ion2}}(t) \tag{51}$$

where the contribution of the antennas is $\phi_{\text{ant}} = \angle a_{\text{vv}} - \angle a_{\text{hh}}$.

The observable phase has a time-dependent systematic variation as the RO sets in addition to the expected hydrometeor phase-shift vertical variation. This is due to: 1) the variation in the angle of arrival which gives different values in the antenna coefficients according to the antenna pattern and 2) to the variation in the ionospheric path when the propagation is not circular. The $\phi_{\text{ant}}(t)$ variation can be completely corrected assuming that we will have knowledge of the copolar parameters of the antenna a_{hh} and a_{vv} for all the angles of arrival. Therefore, we define the antenna-calibrated phase as

$$\phi_{\text{cal}}(t) = \phi_{\text{obs}}(t) - \phi_{\text{ant}}(t) = \phi_{\text{arc}} + \angle \chi_{\text{ion2}}(t). \tag{52}$$

The calibrated phase still contains the effect of the receiver initial phase ϕ_{arc} and the effect of ionosphere in case of an elliptic initial transmission and needs to be corrected and separated from the hydrometeor-dependent term.

B. Phase-Polarimetric Isolation of Precipitation Phase Shift

1) Linearization of the Relative Polarization Phase: To isolate $\Phi_{\text{dp}}(t)$ first, we linearize $\angle \chi_{\text{ion2}}(t)$ in a similar way seen in (34). At this time, there is the additional term $me^{j\theta}$

$$
\begin{aligned}
\angle \chi_{\text{ion2}} &= \frac{\pi}{2} + \arg\left(\frac{1 - pe^{j2\Omega_2} - me^{j\theta}}{1 + pe^{j2\Omega_2} + me^{j\theta}} \right) \\
&= \frac{\pi}{2} + \arctan\left[\frac{-2\,\text{Im}\left[pe^{j2\Omega_2} + me^{j\theta}\right]}{1 - |pe^{j2\Omega_2} + me^{j\theta}|^2} \right]. \tag{53}
\end{aligned}
$$

We are going to consider a negligible dichroism from now on, so that we assume $p = -j\tan(\Phi_{\text{dp}}/2)$.
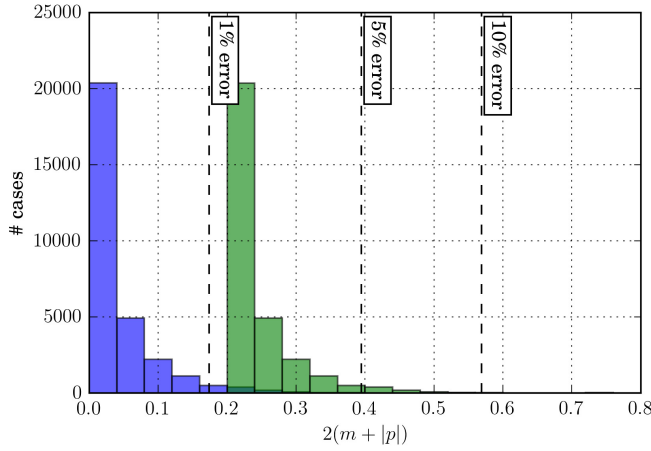
Fig. 6. Statistic distribution of the numerical condition to approximate (55) based on realistic simulations. The histograms follow the distribution of $|p| = \tan(\Phi_{dp}/2)$ according to the histogram in Fig. 2, and the numerical condition is evaluated for two fixed values at $m = 0$ (blue area) and $m = 0.1$ (green area), the latter the worst case. The displayed thresholds are set at values which give the indicated relative error committed in the approximation.

Equation (53) can be linearized provided two conditions. The first is given as the worst case when the terms of $\angle\chi_{ion2}^c$ in (48) sum in-phase, so that

$$m^2 + |p|^2 + 2m|p| \ll 1 \tag{54}$$

which gives $\angle\chi_{ion2} \approx \pi/2 + \arctan(2|p|\cos 2\Omega_2 - 2m\sin\theta)$ instead of getting an exact expression as in (34), and the second is

$$2(m + |p|) < 0.175, 0.55 \tag{55}$$

which is the small-angle approximation for $\arctan x \approx x$ with an error lesser than 1% and 10%, respectively. Thus, the linearization results into

$$\angle\chi_{ion2}(t) \approx \frac{\pi}{2} + \cos 2\Omega_2(t)\Phi_{dp}(t) - 2m\sin\theta(t)$$
$$\approx \frac{\pi}{2} + \left[1 - 2\Omega_2^2(t)\right]\Phi_{dp}(t) - 2m\sin\theta(t) \tag{56}$$

where we can additionally apply the small-angle approximation to $\cos 2\Omega_2$.

For the possible values of m and $|p|$, the most restrictive condition is (55) so the values that verify it also verify (54). The validity of the linearization according to some permitted errors is assessed in Fig. 6. The histogram of $2(|p| + m)$ considers the statistics of p according to Fig. 2, while it is shifted by the value of m: 0 and 0.1, the latter the worst case. Assuming the worst case of m, 97% of events present errors ≤5% in the approximation of the arctangent, while this error tolerance is practically fulfilled for the ideal case of $m = 0$.

2) Subtraction of the Dry Component: We can define the "dry" component phase as those terms of the calibrated phase with no relation to hydrometeor content. From (52) and (56)

$$\phi_{dry}(t) = \phi_{arc} + \frac{\pi}{2} - 2m\sin\theta(t) \tag{57}$$

which includes the constant terms of receiver differential phase and the transmitter phase term $2m\sin\theta(t)$. Any residual effect

of a nonperfect calibration and nonlinearity of χ_{ion2} are also implicitly included here.

Then, using (56) and (57), we divide the calibrated phase profile depending on the presence of hydrometeors in a simple way

$$\phi_{cal}(t) = \begin{cases} \phi_{dry}(t), & t < t_t \tag{58a} \\ \phi_{dry}(t) + \left[1 - 2\Omega_2^2(t)\right]\Phi_{dp}(t), & t > t_t \tag{58b} \end{cases}$$

which shows that the dry term has to be subtracted for the region $t > t_t$, where t_t is the time of the ray with the tangent point at altitude h_t.

To do this, $\phi_{dry}(t)$ has to be extrapolated estimating the trend of the calibrated phase for $t_s < t < t_t$, taking into account the smooth variation of the ionospheric rotation angle $\Omega(t)$, responsible for the only possible time variation along the phase profile not related to hydrometeors.

If we apply the small-angle approximation to $\Omega(t)$, the transmitter phase term of $\phi_{dry}(t)$ results

$$2m\sin\theta(t) = 2m\sin\Delta\cos 2\Omega(t) + 2m\cos\Delta\sin 2\Omega(t)$$
$$\approx 2m\sin\Delta[1 - 2\Omega^2(t)] + 4m\cos\Delta\,\Omega(t). \tag{59}$$

Assuming a linear variation of the rotation angle $\Omega(t) = \Omega_0 + \Omega't + o(t^2)$, (59) is converted into a second-order polynomial as a function of t. Consequently, $\phi_{dry}(t)$, which merely adds two constant terms, is a second-order polynomial as well

$$\phi_{dry}(t) = at^2 + bt + c, \quad t > t_s. \tag{60}$$

We can set a region free of hydrometeors for an interval $[t_a, t_b]$, such that $t_s \leq t_a < t < t_b \leq t_t$, where the fit of the profile can be made and extrapolate it for $t > t_t$. The chosen values have been those corresponding to tangent point heights between 18 and 70 km, which grant little influence of the ionospheric lowest layers and avoid any high layer of hydrometeors at any point of the trajectory.

The hydrometeor phase term that results in the subtraction is identified as the estimator of the phase shift

$$\phi_{hydro}(t) = \phi_{cal}(t) - (\hat{a}t^2 + \hat{b}t + \hat{c}) \tag{61}$$
$$= \left[1 - 2\Omega_2^2(t)\right]\Phi_{dp}(t). \tag{62}$$

Notice that while the impact of the transmitter ellipticity is corrected, the estimate is still dependent on the unknown value of the rotation posttroposphere Ω_2. Therefore, the larger the rotation angle Ω_2 is, the less accurate the estimate of ϕ_{hydro} will be.

C. Dual-Frequency, Phase-Polarimetric Isolation of Precipitation Phase Shift

In this section, the proposed method combines the phase observables at two frequency bands, L1 and L2 or L5, to separate the ionospheric influence from the estimation of Φ_{dp}. The dual-frequency method offers a chance to completely remove the ionospheric effect and to estimate it. However, it may be difficult to implement at the ROHP-PAZ experiment because of lower performance of the L2 observable and cross-polar antenna isolation.

Both ionospheric and hydrometeor parameters are frequency-dependent. Given a couple of frequencies f_1 and f_2

at L-band, on one hand, the polarimetric phase shift Φ_{dp} validates the relationship

$$\frac{\Phi_{dp}(f_1)}{f_1} = \frac{\Phi_{dp}(f_2)}{f_2} \tag{63}$$

for all potentially expected Φ_{dp} and rain rates.

On the other hand, the rotation angle is proportional to f^{-2}. Thus, we get the relationship

$$f_1^2 \Omega_2(f_1) = f_2^2 \Omega_2(f_2). \tag{64}$$

Applying the small-angle approximation to the frequency (63) and (64), an equation system is made to estimate both the phase shift and the rotation angle

$$\begin{cases} \phi_{hydro}(f_1) = \left[1 - 2\Omega_2^2(f_1)\right] \Phi_{dp}(f_1) & \text{(65a)} \\ \phi_{hydro}(f_2) = \frac{1}{\nu}\left[1 - 2\nu^4 \Omega_2^2(f_1)\right] \Phi_{dp}(f_1) & \text{(65b)} \end{cases}$$

where $\nu = f_1/f_2$.

Then, the estimation for $\Phi_{dp}(f_1) \neq 0$ is given by

$$\hat{\Phi}_{dp}(f_1, t) = \frac{\nu^4 \phi_{hydro}(f_1, t) - \nu \phi_{hydro}(f_2, t)}{\nu^4 - 1}. \tag{66}$$

On the other hand, the estimation for the ionospheric rotation angle is also obtained by

$$\Omega_2(f_1, t) = \pm \left[\frac{1}{2} \frac{\phi_{hydro}(f_1, t) - \nu \phi_{hydro}(f_2, t)}{\nu^4 \phi_{hydro}(f_1, t) - \nu \phi_{hydro}(f_2, t)}\right]^{\frac{1}{2}} \tag{67}$$

where its rotation sense cannot be determined but just its absolute value.

This method assumes that, although the dispersion gives different paths to the trajectories for the same time t, their Fresnel volumes are overlapped enough not to convey meaningful differences between the zones they cross. This is not a significant limitation, since historically, the GNSS and RO communities use a dual-frequency combination to estimate the properties of the ionosphere, assuming this closeness of paths.

VII. Results and Discussion

To assess the accuracy of the Φ_{dp} isolation, both algorithms of Section VI have been applied to the collection of 550 RO profiles collocated with precipitation events for a total of $\sim$30 000 detected precipitation affected rays. The input values for the transmitter have been set as $m = 0.1$, equivalent to 1.8 dB of ellipticity, which is the worst case scenario expected at the L1 band, and Δ varying from 0 to π in the intervals of $\pi/4$.

Fig. 7 shows the absolute error $\epsilon_{abs} = \Phi_{dp} - \hat{\Phi}_{dp}$ in the estimation of Φ_{dp}. The estimation $\hat{\Phi}_{dp}$ is obtained using a single-frequency observable: L1 for the left column and L2 for the central column. The dual-frequency method described in Section VI-C is applied on the right column to obtain an estimation at the L1 frequency. Each row corresponds to a different initial phase of the transmitter Δ. The plots are made as a function of the posttropospheric rotation angle Ω_2, where each dot is colored according to a scale which shows the actual value of Φ_{dp}.

We found that the 95% of cases are contained for $\Omega_2(f_{L1}) < 14°$ (equivalently, $\Omega_2(f_{L2}) < 22°$). The remaining

5% of cases correspond to higher and less frequent values of the posttroposphere rotation angle Ω_2.

A. Single-Frequency Estimation

Considering the single-frequency estimation, for the majority of cases, the worst deviation is less than 1.5 mm, which is of the same order of magnitude as the expected noise. As Ω_2 increases, the error increases, showing an envolvent effect of the factor $\cos 2\Omega_2 \approx 1 - 2\Omega_2^2$. The plot indicates that the highest deviations or outliers appear either by very high precipitation events without particularly high angles (e.g., 20 mm at 7° of rotation) or by high angles of rotation without particularly high precipitation phase shifts (e.g., ROs points of 6–10 mm at rotations between 20° and 25°). Almost all significant deviations at medium or large rotation angles have a positive value, which represents an underestimation.

For L2 band, it can be seen that, for the same distribution of cases, the angular factor effect is amplified because of the scaling relation between rotations [see (64)]. This worsens the absolute error. This is particularly evident in the outliers of some particular ROs but also in the distribution of cases with a low rotation angle, which present larger spread. Thus, L1 is the most suitable GNSS frequency to rely on and consider L2 just as a complementary measurement.

In Fig. 7, there is an evidence of a dependence of the retrieval accuracy on Δ. The value of Δ affects the residual in the subtraction of the free-atmospheric fit of (61) and the estimation of ϕ_{hydro}. We can assess this impact looking at (59), where there is a linear combination of the rotation angle with $\sin \Delta$ and $\cos \Delta$ as weights. The small-angle approximations for $\sin 2\Omega$ and $\cos 2\Omega$ depend on $\cos \Delta$ and $\sin \Delta$, respectively. The best accuracy is obtained for $\Delta = \pm\pi/2$ (equivalent to an initially oriented ellipse of $\pm\pi/4$) which only takes the approximation $\cos 2\Omega \approx 1 - 2\Omega^2$ in the fit. The small-angle approximation is valid for larger values of Ω for the cosine than for the sine. Hence, at $\Delta = \pm\pi/2$, the fit would have a lesser residual for both L1 and L2 ϕ_{hydro} estimations than for other values. This translates to a better estimation of Φ_{dp} for a wider range of Ω_2 values.

The majority of cases have a small rotation angle as well as low values of Φ_{dp}. To reveal better, the distribution of the absolute error of these cases than in Figs. 7 and 8 plots only the 95th percentile of cases for the three frequencial scenarios (worst 5% errors rejected). The cases are centered around zero with the same amount of overestimation or underestimation. To show the dispersion, the standard deviation is plotted as cumulative error bars in the steps of 2°.

The variation of Δ in Fig. 8 reveals that the dispersion of the error for the best case ($\Delta = \pi/2$) is narrower than for other cases both at L1 (left column) and L2 (central column), in agreement to the explanation for validity of the fit. Hence, for the worst case, at $\Delta = 0$, the error bar reaches 0.07 mm for L1 in a single-frequency estimation (0.1 mm at L2). In comparison, for the best case, the dispersion starts at 0.04 mm (0.09 mm at L2). In addition, for $\Delta = \pi/2$, the dispersion is biased toward underestimation at both frequencies, while cases are more evenly distributed for other values of Δ. These two facts, a narrower dispersion and the underestimation bias,
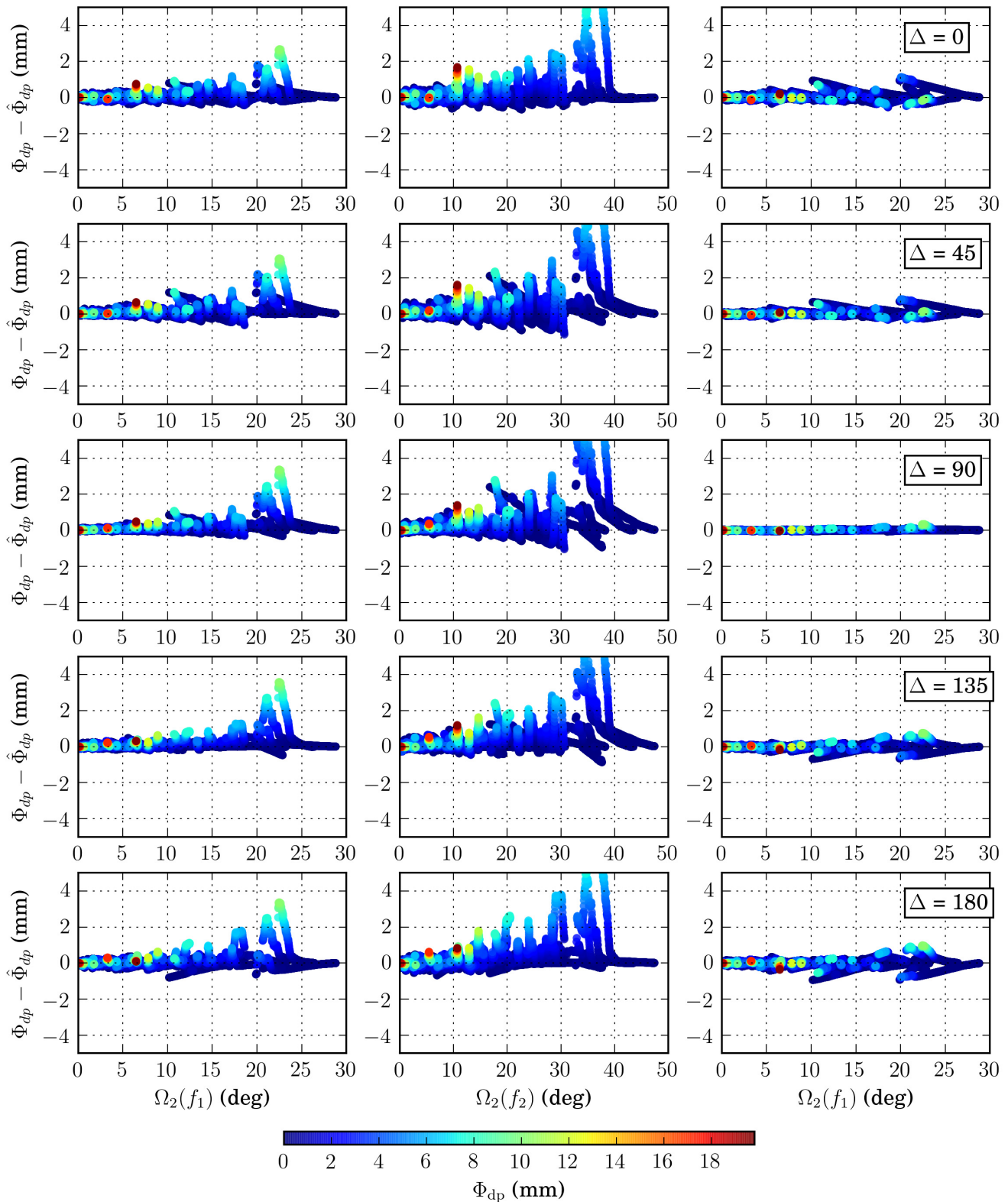
Fig. 7. Absolute error in the estimation of Φ_{dp} in mm as a function of the posttroposphere rotation angle Ω_2. Each row has a different value of Δ, from 0° to 180°, in the steps of 45°. The transmitted ellipticity applied is of 1.8 dB. (Left column) Absolute error at L1 frequency by a single-frequency estimation. (Center column) Absolute error at L2 frequency by a single-frequency estimation. (Right column) Absolute error at L1 frequency by combining L1 and L2 phase observables. The color of the dots indicates the actual value of Φ_{dp} in mm.

may explain why the estimation works better than in other cases where overestimation is more frequent. In either way, these error levels are much smaller than the expected noise level of the measurement (1.5 mm at the bottom layers of the troposphere) and expected heavy rain signatures (several mm up to cm level) [7].
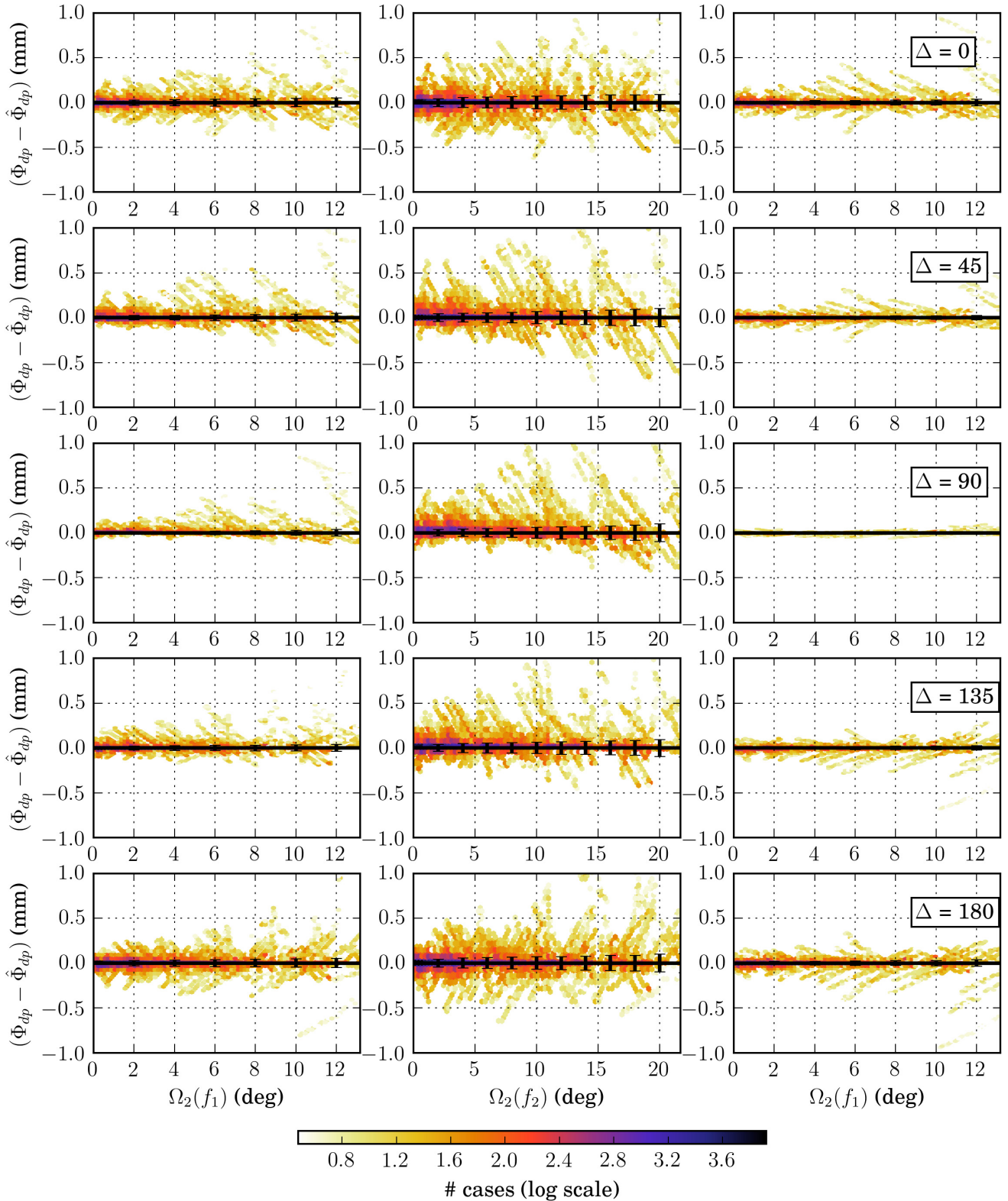
Fig. 8. Distribution of the absolute error for the 95% of cases. Each row is a different value of Δ, from 0° to 180°, in steps of 45°. The transmitted ellipticity is 1.8 dB. (Left column) Error at L1 frequency by a single-frequency estimation. (Center column) Error at L2 frequency by a single-frequency estimation. (Right column) Absolute error at L1 frequency by combining L1 and L2 phase observables. The color shows the amount of cases in a logarithmic scale. Superposed there are the cumulative standard deviations as a function of Ω_2, each 2°.

B. Dual-Frequency Estimation

Regarding the dual-frequency combination, the right column in Fig. 7 illustrates the potential improvement of the estimation of $\Phi_{dp}(f_{L1})$; in this case, both observables were generated under the same transmitter conditions. Thanks to the actual correction of the Ω_2 effect, the deviations due to either a high

TABLE II
Mean and Standard Distribution of the Absolute Error (in mm). It Corresponds to the Ensemble of All the Combinations of $\Delta(f_1)$ and $\Delta(f_2)$ and Worst m Value

Φ_{dp}(mm)	$\bar{\epsilon}_{dual}$	σ_{dual}	$\bar{\epsilon}_{single}$	σ_{single}
< 1.5	0.005	0.151	0.013	0.084
$[1.5, 3)$	0.011	0.196	0.055	0.166
$[3, 4.5)$	0.023	0.268	0.123	0.295
$[4.5, 6)$	-0.021	0.347	0.236	0.459
> 6	-0.007	0.324	0.327	0.672

value of phase shift at L1 or due to high values of rotation angle are all corrected. In particular, the increase of the error amplitude envelop as a function of Ω_2 found in the left and central columns disappears in the right one.

The deviations in the combined method are not completely removed even for the coincident phases. This is due to both the assumed error in the linear approximation and the fit residual required to subtract the "dry" phase component. The right column in Fig. 8 shows a reduction of the dispersion compared with the single-frequency method, where the accumulated standard deviation of the error goes from 0.07 to 0.05 mm for $\Delta = 0$ and from 0.04 to 0.02 mm for $\Delta = \pi/2$. Note that these simulations assumed $\Delta(f_1) = \Delta(f_2)$.

Provided that we lack knowledge about the initial transmission, we need to assume that the initial circular phase shift for L1 and L2 is not necessarily the same: generally, $\Delta(f_1) \neq \Delta(f_2)$. In addition, we assume that the initial phases are uncorrelated and randomly uniform. Under these assumptions, we simulated all the possible combinations of $\Delta(f_1)$ and $\Delta(f_2)$ with the previous values assigned to Δ. We found that for every combination, the distribution of the absolute error is centered to zero and independent on the value of Ω_2, just as in the example of the right column in Fig. 7.

When the values of Δ are different between frequencies, there is a different dependence of the residuals at each frequency, and the Ω_2-correction proposed in (66) becomes suboptimal in terms of dispersion. The potential impact of the unknown transmitter state into the retrieved phase errors is summarized in Table II, which shows the mean and standard deviations of the absolute error of estimation obtained from the ensemble of all the combinations of $\Delta(f_1)$ and $\Delta(f_2)$; therefore, these statistics show the expected bias and dispersion of the error *on average*, without knowing *a priori* the initial transmitter Δ and made for the worst case of ellipticity. The statistics are classified into arbitrary intervals of the actual phase shift. For comparison, the same statistics have been made for the single-frequency estimation at L1, using the five plots of the left column in Fig. 7.

The mean and standard deviation for the single-frequency method consider the underestimations made by the rotation angle and, hence, the nonzero bias. To the contrary, this is not present in the dual-frequency method that shows the improvement of the estimation. The standard deviation also accounts for those cases of high rotation, not only for those shown in Fig. 8. Thus, it can be seen that as the phase shift

increases, the dispersion of the estimation error also increases for both methods, but it is higher for the single-frequency method in agreement with the noncorrected rotation angle effect. There are no cases where the standard deviation is higher than the expected noise dispersion of 1.5 mm for RO trajectories at the bottom kilometer of the troposphere.

We can conclude that the differential polarimetric phase measurement is a valid method that overcomes the impracticality of having full-polarimetric observables at heights where precipitation is expected. The single-frequency approach estimates well many events despite the lack of complete separability between geophysical parameters. It presents underestimation cases when the rotation angle increases, yet they conform a minority of events. The dual-frequency approach is potentially able to correct these exceptions by a proper separation and estimation of both Φ_{dp} and Ω_2. The lack of knowledge on the initial transmission phases deprives the proposed method to be optimal for each possible RO event, yet its performance presents a nonbiased estimation and less dispersion than in the single-frequency approach. In addition, the complete separation of the posttropospheric rotation angle opens new possibilities for ionospheric-related measurements, which are beyond the scope of this paper.

VIII. CONCLUSION

A reliable method to detect the effect of precipitation events using polarimetric GNSS radio occultations has been demonstrated feasibly. It relies solely on polarimetric phase observables instead of both amplitude and phase. It has been possible to estimate the induced phase shift term that can be related to rain rate in tropospheric-sounding RO rays. Accordingly, several potential threats affecting the measurement have been identified.

The methodology in this paper has consisted in performing an analysis of the end-to-end forward propagation of the coherent electric field from a GNSS transmitter toward a polarimetric LEO receiver. Then, the polarization changes experimented along the path has been accounted. The impact of several systematic effects has been assessed: the phase shift and differential attenuation from a hydrometeor layer, the Faraday rotation of the ionosphere, the ellipticity of a nonideal transmission, and the receiver parameters. For those effects of atmospheric origin, it has been considered not only the maximum possible values but also their statistical distribution by means of a database of colocated ROs with precipitation-measurement satellites and using numerical models for the ionosphere and the earth's magnetic field.

At L-band, hydrometeors essentially affect the polarimetric phase (phase shift) that is the selected observable for the ROHP-PAZ experiment. For an RH circular incident field, the phase shift causes a variation in its ellipticity with an invariant rotation of $-45°$. The differential attenuation could potentially affect the phase shift, but it has been here proven that it only causes an RH rotation of $0.2°$ as a maximum and for a very few cases. Therefore, the effects of the differential attenuation into the phase shift are deemed negligible under the GNSS PRO conditions. In this paper, the role of horizontal

ice crystals has not been considered due to the variability of the magnitude of the phase shift they can provide, becoming an extra source of uncertainty. Future studies and techniques will have to deal with the effect of possibly integrated ice clouds from the integrated precipitation path.

The method here developed relies on several assumptions that have been demonstrated statistically valid. In the first place, the ionospheric rotation effect is significant at L-band, yet the collocation and simulation exercise proved that its expected range of values for a moderate activity of the ionosphere allow small-angle approximations. These approximations have also been proven valid for the raindrop-induced phase shift.

In the second place, the ellipticity in the GNSS transmission has been considered. Its effect is comparable to that of the hydrometeors in the circular relative phase of the field. However, the sum of both terms still allows a linear approximation to the measured polarimetric differential phase for a 97% of potential cases with a relative error of $\leq 5\%$. This feature permits to develop a simple correction of transmitter-based effects.

Finally, for rays below 100 km (tangent point height reference), we proved statistically feasible to assume a smooth variation of the vertical profile of the integrated rotation angle. This feature enables a polynomial fit of the differential phase in a hydrometeor-free region as a simple method to separate the hydrometeor-based phase contribution from the rest of effects.

The impact of an unknown initial orientation for a nonpurely RHCP transmission has been explicitly studied. It has been observed that the best estimation of the phase shift happens at $\Delta = \pm\pi/2$ and the worst at $\Delta = 0, \pm\pi$. However, the statistics demonstrate that all its possible values fit into a second-order profile for the observable phase, and hence, the method is suitable for all cases.

The linear approximation of the differential polarimetric phase allows the correction of most of the effects but cannot separate completely the impact of the posttropospheric Faraday rotation, which remains as the most influential parameter after phase-correction procedures. To completely separate its effect, a second frequency observable has been proposed using both L1 and L2 bands. The simulations have shown that the dual method has the potential to separate effectively the phase shift, improving the deviations found in the estimation using the single-frequency method under the presence of high Faraday rotation angles. The unknown values of both initial phases (Δ at L1 and L2) in the transmission cause an estimation dispersion of just 0.3 mm on average, for those cases of $\Phi_{dp} > 6$ mm, considered the most relevant for rain detectability, which is fairly below the expected sensitivity limitation caused by the noise, around 1.5 mm.

The relatively simple methodology on the ray tracing for the RO trajectories may hide some unexpected effect. In this regard, only actual data will determine the validity of the model approximation in this paper. There is the possibility of including in the future additional methods of analysis such as radio holograms on each polarization to discern factors such as the multipath, which may open new research opportunities.

In the same line of thought, the averaged models for the ionosphere modeling may underestimate the relative frequency of extreme rotation angle values, which is still presumably lower than the moderate values. Short-term ionosphere models should clarify the role of the rotations more than in their current state, and new methods should handle these events to detect and correct them when present.

Other aspects to consider in the future are related to the improvement of the correction fit and to develop new procedures to extract information about the transmitter parameters. Some aspects out of the scope of this paper are the cross polarization by mean canting angles or the effect of the canting variance, which should have a potential influence in scenarios other than windless rain. The role of ice crystals in the polarimetric signature has to be characterized and separated from the precipitation, potentially using the additional information provided by the GNSS RO measurement itself (e.g., temperature) or by other sources. In addition, it has been hinted that the posttropospheric rotation angle can be estimated by the dual-frequency method, and this allows new possibilities of ionospheric sounding as a complementary feature of the GNSS PRO technique.

REFERENCES

[1] A. Steiner, B. Pirscher, U. Foelsche, and G. Kirchengast, Eds., *New Horizons in Occultation Research*. Berlin, Germany: Springer-Verlag, 2009.
[2] S. Jin, E. Cardellach, and F. Xie, *GNSS Remote Sensing. Theory, Methods and Applications*. Dordrecht, The Netherlands: Springer, 2014.
[3] J. R. Eyre, "An introduction to GPS radio occultation and its use in numerical weather prediction," in *Proc. ECMWF GRAS SAF Workshop Appl. GPS Radio Occultation Meas.*, 2008, pp. 1–10.
[4] S. B. Healy, "Forecast impact experiment with a constellation of GPS radio occultation receivers," *Atmos. Sci. Lett.*, vol. 9, pp. 111–118, 2008.
[5] L. Cucurull, "Improvement in the use of an operational constellation of GPS radio occultation receivers in weather forecasting," *Weather Forecasting*, vol. 25, pp. 749–767, Apr. 2010.
[6] M. P. Rennie, "The impact of GPS radio occultation assimilation at the met office," *Quart. J. Roy. Meteorol. Soc.*, vol. 136, no. 646, pp. 116–131, Jan. 2010.
[7] E. Cardellach *et al.*, "Sensitivity of PAZ LEO polarimetric GNSS radio-occultation experiment to precipitation events," *IEEE Trans. Geosci. Remote Sens.*, vol. 53, no. 1, pp. 190–206, Jan. 2015.
[8] R. Padullés *et al.*, "Atmospheric polarimetric effects on GNSS radio occultations: The ROHP-PAZ field campaign," *Atmos. Chem. Phys.*, vol. 16, no. 2, pp. 635–649, 2016.
[9] E. R. Kursinski, G. A. Hajj, J. T. Schofield, R. P. Linfield, and K. R. Hardy, "Observing Earth's atmosphere with radio occultation measurements using the Global Positioning System," *J. Geophys. Res.*, vol. 102, no. D19, pp. 23429–23465, 1997.
[10] A. Ishimaru and R. T. Cheung, "Multiple scattering effects on wave propagation due to rain," *Ann. Télécommun.*, vol. 35, nos. 11–12, pp. 373–379, 1980.

[11] V. N. Bringi and V. Chandrasekar, "Wave, antenna, and radar polarization," in *Polarization Doppler Weather Radar: Principles and Applications*. Cambridge, U.K.: Cambridge Univ. Press, 2001, pp. 89–159.

[12] H. Mott, "Definitions of polarization in radar," in *Direct and Inverse Methods in Radar Polarimetry* (NATO ASI Series), W. M. Boerner *et al.*, Eds. Dordrecht, The Netherlands: Springer, 1992, pp. 117–151.

[13] H. C. Van De Hulst, *Light Scattering by Small Particles*. New York, NY, USA: Wiley, 1981.

[14] V. N. Bringi and V. Chandrasekar, "The polarimetric basis for characterizing precipitation," in *Polarization Doppler Weather Radar: Principles and Applications*. Cambridge, U.K.: Cambridge Univ. Press, 2001, pp. 378–532.

[15] V. N. Bringi, M. Thurai, and D. A. Brunkow, "Measurements and inferences of raindrop canting angles," *Electron. Lett.*, vol. 44, no. 24, pp. 1425–1426, Nov. 2008.

[16] T. S. Chu, "Rain-induced cross-polarization at centimeter and millimeter wavelengths," *Bell Syst. Tech. J.*, vol. 53, no. 8, pp. 1557–1579, Oct. 1974.

[17] T. Oguchi, "Scattering properties of Pruppacher-and-Pitter form raindrops and cross polarization due to rain: Calculations at 11, 13, 19.3, and 34.8 GHz," *Radio Sci.*, vol. 12, no. 1, pp. 41–51, Jan./Feb. 1977.

[18] R. L. Olsen, "A review of theories of coherent radio wave propagation through precipitation media of randomly oriented scatterers, and the role of multiple scattering," *Radio Sci.*, vol. 17, no. 5, pp. 913–928, Sep./Oct. 1982.

[19] E. Cardellach, R. Padullés, S. Tomás, F. J. Turk, C. O. Ao, and M. de la Torre-Juárez, "Probability of intense precipitation from polarimetric GNSS radio occultation observations," *Quart. J. Roy. Meteorol. Soc.*, 2017, doi: 10.1002/qj.3161.

[20] A. J. Mannucci, C. O. Ao, X. Pi, and B. A. Iijima, "The impact of large scale ionospheric structure on radio occultation retrievals," *Atmos. Meas. Tech.*, vol. 4, pp. 2837–2850, 2011.

[21] R. D. Hunsucker and J. K. Hargreaves, "Fundamentals of terrestrial radio propagation," in *The High-Latitude Ionosphere and its Effects on Radio Propagation*. Cambridge, U.K.: Cambridge Univ. Press, 2003, pp. 113–180.

[22] K. C. Yeh, H. Y. Chao, and K. H. Lin, "A study of the generalized Faraday effect in several media," *Radio Sci.*, vol. 34, no. 1, pp. 139–153, Jan./Feb. 1999.

[23] D. Bilitza *et al.*, "The International Reference Ionosphere 2012—A model of international collaboration," *J. Space Weather Space Clim.*, vol. 4, Feb. 2014, Art. no. A07.

[24] E. Thébault *et al.*, "International Geomagnetic Reference Field: The 12th generation," *Earth, Planets Space*, vol. 67, p. 79, Dec. 2015.

[25] Global Positioning System directorate. (Jul. 2016). *Systems Engineering & Integration. Interface Specification IS-GPS-200 (Revision H, IRN003)*, p. 21. [Online]. Available: http://www.gps.gov/technical/icwg/

[26] Global Positioning System directorate. (Sep. 2013). *Systems Engineering & Integration. Interface Specification IS-GPS-705D*, p. 11. [Online]. Available: http://www.gps.gov/technical/icwg/

Sergio Tomás received the Ph.D. degree in telecommunications engineering from the Universitat Politècnica de Catalunya, Barcelona, Spain, in 2010. He did his M.Sc. thesis in telecommunications engineering at the Institute of Photonic Sciences, Barcelona.

In 2012, he joined the Institute of Space Sciences, CSIC, Barcelona, Spain, as a Research Engineer, where he was involved in the detection of precipitation with polarimetric Global Navigation Satellite System (GNSS) radio occultations. Since 2007, he has been with the Institute of Estudis Espacials de Catalunya, Barcelona. His research interests include atmospheric remote sensing, atmospheric LiDAR systems, wind monitoring, boundary layer detection algorithms, and the calibration and data retrieval of GNSS radio occultations for heavy precipitation detection.

Ramon Padullés received the Ph.D. degree in physics from the University of Barcelona, Barcelona, Spain, for his research on polarimetric radio occultations at the Institut de Ciéncies de l'Espai, CSIC, Barcelona.

He is currently a NASA Post-Doctoral Program Fellow with the Jet Propulsion Laboratory, Pasadena, CA, USA. He is involved with the Radio Occultation and Heavy Precipitation aboard PAZ satellite mission developing calibration/validation and data analysis algorithms. His research interests include the study of extreme precipitation using radio occultation technique and the applications of polarimetric radio occultations.

Estel Cardellach (M'10) received the Ph.D. degree in physics from the Technical University of Catalonia, Barcelona, Spain, in 2002.

She held a post-doctoral position at the NASA/Jet Propulsion Laboratory, Pasadena, CA, USA, as a National Research Council Awardee from 2002 to 2003, and a Post-Doctoral Researcher at the Harvard–Smithsonian Center for Astrophysics, Cambridge, MA, USA, from 2003 to 2005. Since 2005, she has been with the Institute of Space Sciences, CSIC, Barcelona, and the Institute of Estudis Espacials de Catalunya, Barcelona. She is currently the Principal Investigator of the space-borne experiment Radio-Occultation and Heavy Precipitation aboard the PAZ low earth orbiter. She has been involved in the scientific applications of Global Navigation Satellite Systems (GNSSs) for remote sensing of the earth, such as extraction of geophysical information of the GNSS reflected signals, radio occultation, and geodetic techniques.